NJC

ROYAL SOCIETY OF CHEMISTRY

PAPER

View Article Online
View Journal

Cite this: DOI: 10.1039/d6nj00232c

Enhanced titanium carbide MXene structure with CuO quantum dots as an electrode for advanced supercapacitor applications

Mpho Rantsotlhe,[a] Kabir Otun,[a] Rashed A. M. Adam,[a] Gift Rutavi,[a] Samuel Chigome[b] and Ncholu Manyala *[a]

Ti_3C_2 : CuO quantum dot composites with different mass ratios (1 : 0.5, 1 : 1 and 1 : 2) were successfully synthesized through hydrofluoric acid etching of Ti_3AlC_2 (MAX phase) to obtain Ti_3C_2 MXene, followed by sonication-assisted intercalation of quantum dots. The incorporation of CuO quantum dots was found to effectively prevent MXene restacking, enhance ion accessibility, and introduce additional redox-active sites, thereby improving the electrochemical properties of the electrode material. Among the tested composites, the Ti_3C_2 : CuO QDs (1 : 1) composite delivered the highest specific capacitance of 108.1 F g^{-1} in a three-electrode configuration, significantly outperforming pristine Ti_3C_2 (74.2 F g^{-1}) in 1 M H_2SO_4. An asymmetric supercapacitor (SC) device was further fabricated using Ti_3C_2 : CuO QDs (1 : 1) as the negative electrode and human hair-derived activated carbon as the positive electrode. The device exhibited a high coulombic efficiency of 94.8%, excellent cycling stability with 82.6% capacitance retention after 10 000 cycles, a specific energy of 5.4 W h kg^{-1}, and a power density of 410 W kg^{-1} at 1 A g^{-1}. These findings highlight the synergistic benefits of CuO quantum dot intercalation and confirm the promise of Ti_3C_2 : CuO QDs composites as advanced electrode materials for high-performance supercapacitors.

Received 21st January 2026,
Accepted 31st March 2026

DOI: 10.1039/d6nj00232c

rsc.li/njc

1. Introduction

There is a global transition from fossil fuel-based energy systems toward renewable energy options, which are generally considered more sustainable and less polluting than fossil fuels, which are the main contributors to greenhouse gas emissions and climate change. Fossil fuel emissions have been strongly linked to an observed rise in the Earth's average surface temperature, estimated at 1.1 °C,[1] which poses a threat to natural habitats.[2] However, there has been a transition toward safer energy sources such as solar, wind, geothermal, and others, which contributed approximately 18% to electricity generation in 2023 and 2024.[3,4] These sources are generally intermittent depending on weather conditions, seasonal variations, and yearly fluctuations. Therefore, energy storage systems are essential to ensure a stable supply of electricity when required.[5] Such systems serve multiple functions, including supporting network operation and maintaining load balance, for example, by (i) helping in meeting peak electrical load demands, (ii) providing time varying energy management, (iii) alleviating the intermittence of renewable source power generation, (iv) improving power quality/reliability, (v) meeting remote and vehicle load needs, (vi) supporting the realization of smart grids, (vii) helping with the management of distributed/standby power generation and (viii) reducing electrical energy import during peak demand periods.[5]

These energy storage systems include supercapacitors (SCs), batteries, and fuel cells.[4] Batteries possess high specific energy,[6] which makes them superior to supercapacitors; however, batteries are known to contain toxic materials and generate hazardous waste; moreover, their high maintenance costs, low specific power, and limited lifespan[7] significantly constrain their performance as energy storage devices. Consequently, their application in systems requiring instantaneous power delivery, such as emergency backup mechanisms in airplane doors and elevators, remains inadequate for addressing such high-power demands. This limitation highlights the potential of supercapacitors as alternative or complementary energy storage systems, as they offer substantially higher specific power, longer cycle life, and lower maintenance requirements compared to conventional batteries.[8] Those advantages, however, come with certain trade-offs. Despite their remarkable

[a] Department of Physics, SARCHI Chair in Nanomaterials for Energy storage and Water Purification, University of Pretoria, 0002, Pretoria, South Africa. E-mail: ncholu.manyala@up.ac.za
[b] Department of Natural Resources and Materials, Nanomaterials Division, Botswana Institute for Technology Research and Innovation, Gaborone, Botswana

specific power and long cycle stability, supercapacitors are primarily constrained by their low specific energy. As shown in eqn (1), the specific energy (E_s) scales with both the specific capacitance (C_s) and the square of the operating voltage (V),[9] and therefore, in practice, the attainable values of these parameters limit the total energy that can be stored compared to batteries.

$$E_s = \frac{1}{2} C_s V^2 \quad (1)$$

Enhancing either of the two key parameters (the specific capacitance or the operating voltage) directly increases the specific energy of a supercapacitor. Consequently, the development of cost-effective electrode materials with superior electrochemical properties is vital for improving the specific capacitance and, overall, the energy density of the device. The rational design of electrode materials requires careful consideration of several factors, including the ionic size and diffusion behavior of electrolyte species, the chemical and structural stability of the electrode, and its effective surface area available for charge storage.[10] In parallel, the electrolyte plays an equally critical role in determining device performance. An ideal electrolyte should possess wide electrochemical stability, high ionic conductivity, low cost, good thermal stability, and a broad operating potential window.[11,12] Therefore, achieving optimal performance necessitates a well-matched electrode–electrolyte pair tailored to the intended application in supercapacitors.

Given these attributes, supercapacitors are projected to experience significant growth in demand across multiple technological fields. Their implementation is increasingly recognized in advanced applications such as frequency regulation, regenerative braking, and energy recovery systems within grid-connected transportation networks, including light rail systems.[13,14] The most popularly used material to synthesize electrodes is carbon, which exhibits electric double-layer capacitance (EDLC) and is very porous, accommodating a variety of electrolytes.[13] However, its charge storage is restricted to surface-level interactions between the electrode and electrolyte, relying solely on the EDLC mechanism.[14] This is less efficient compared to hybrid materials, which integrate both EDLC and fast reversible faradaic processes arising from electroactive species known as pseudo-capacitance.[14,15] Typically, such hybrid materials are engineered by combining carbon-based materials with pseudocapacitive components such as metal oxides, conducting polymers, or metal carbides to achieve synergistic improvements in energy storage performance. Titanium carbide is a popularly used metal carbide, generally known as MXenes, which is a 2D carbide of transition metals. It can be produced by selective etching of strongly bonded layered solids.[16–18] Depending on the etching strategy, hydrofluoric acid (HF) is commonly employed for MXene synthesis. However, owing to its highly corrosive and hazardous nature, modified approaches have been introduced, such as using diluted HF in combination with weaker acids to enhance the safety and controllability of the process.[19] MXenes, generally expressed using the formula $M_{n+1}X_nT_x$ (where M represents an early transition metal, X is carbon and/or nitrogen, and T_x denotes surface terminations), are typically synthesized through HF etching of their precursor MAX phases. This process yields highly conductive MXene with high yield; however, the outcome is strongly influenced by several factors, including the nature of surface terminations,[20] the efficiency of the removal of A (aluminum (Al) in this case) from the parent MAX phase (Ti_3AlC_2), and the degree of exfoliation, which governs ion accessibility and interaction with the material's active sites. Delaminated titanium carbide MXene, in general, is highly conductive, chemically stable, and has a remarkably high surface area.[21,22] It has its own drawbacks, including restacking of layers after etching, poorly conducting functional groups, and easy oxidation in aqueous solution, which degrades its electrical conductivity and structural integrity.[20,21] Some studies attempted to overcome these problems by doping with oxides and nitrogen nanoparticles, achieving a specific capacity of 128 mA h g^{-1} and a capacitance of 246 F g^{-1},[23,24] while others modified parameters such as the time of etching and the drying approach used to optimize them.[25]

Inspired by the above considerations,[24,26] this work employs HF selective etching (because of its benefits), intercalates layers of titanium carbide with copper oxide (CuO) quantum dots to create more passage for ions (*i.e.* prevent restacking), and modifies the surface of The Ti_3C_2 by creating a thin layer of insulation that also passivates defects to reduce trap states of charges, thus increasing electrical conductivity and reducing chances of oxidation on the surface of the material. The synthesis of CuO quantum dots and Ti_3C_2 is independent of each other, meaning that after etching the MAX phase to obtain the pristine Ti_3C_2 MXene, it is sonicated to delaminate the layers, and CuO quantum dots are added so that the restacking happens with quantum dots intercalated and glued to the surface of the layers. The electrode was electrochemically active in 1 M H_2SO_4 when tested at a negative potential, with different mass ratios of mixing of 1 : 0, 1 : 1, and 1 : 2 for Ti_3C_2 : CuO QDs. The 1 : 1 ratio performed the best, reaching the highest specific capacitance (108.1 F g^{-1}) compared with pristine MXene (74.2 F g^{-1}) in three three-electrode set-ups. Furthermore, a device was fabricated with human hair activated carbon[27] as the positive electrode, achieving an asymmetric device with a columbic efficiency of 94.8% and a capacitance retention of 82.6% after 10 000 cycles at 10 A g^{-1}. It has an equivalent specific energy and a specific power of 5.4 W h kg^{-1} and 410 W kg^{-1} at 1 A g^{-1}, respectively. This work provides insight into engineering of the structures of Ti_3C_2 *via* quantum dots effects for enhanced electrochemical energy storage performance.

2. Experimental details

2.1. Materials

Cupric chloride dihydrate, sodium hydroxide, acetic acid, cetyltrimethylammonium bromide (CTAB), distilled water, ethanol, and hydrofluoric acid purchased from LAB CHEM, and

titanium carbide MAX-phase powder from Drexel Engineering laboratory were used in this study.

2.2. Preparation of CuO quantum dots

CuO quantum dots were synthesized as described in ref. 28 with slight modifications. Cupric chloride (2.04576 g) dihydrate was dissolved in distilled water (600 mL) to obtain a 0.02 M solution and stirred continuously for 10 minutes, then 3.44 mL of acetic acid was added to the solution and agitated under magnetic stirring at room temperature for 5 minutes. Next, (0.9 g) CTAB was added to the mixture, stirred well until complete dissolution, and heated to 50 °C. Then 12 g of sodium hydroxide powder was slowly added to the cupric chloride solution under stirring, maintaining a pH of 10. The mixture was heated, resulting in the formation of copper(II) hydroxide as a black precipitate. It was stirred until the reaction was complete, and the precipitate was allowed to settle. Then the supernatant liquid was decanted, and the precipitate was washed with distilled water and ethanol several times to remove impurities, sonicated for 30 minutes, then centrifuged at 5000 rpm for 5 minutes, and dried in an oven at 100 °C for 4 hours and at 60 °C for 24 hours.

2.3. Preparation of Ti_3C_2 MXene

The MAX-phase powder Ti_3AlC_2 was slowly added to HF acid, which was preheated to 35 °C, and the reaction proceeded for 24 hours at 35 °C in a Teflon vessel placed in a fume hood. To obtain multilayered MXene, the as-prepared sample was washed several times with deionized (DI) water until a pH of 7 was reached and then centrifuged at 4500 rpm for 10 minutes. The resulting pristine MXene was sonicated in NMP for 135 minutes, followed by centrifugation at 4500 rpm for 10 minutes, and subsequently dried at 60 °C for 24 hours in a vacuum oven. Scheme S1 in the SI elaborates more on the synthesis.

2.4. Preparation of Ti_3C_2–CuO quantum dots (QDs) composites

Ti_3C_2/CuO QDs composites were prepared at different mass ratios of Ti_3C_2 to CuO QDs (1 : 0.5, 1 : 1, and 1 : 2). For example, for the 1 : 1 ratio, 100 g of Ti_3C_2 and 100 g of CuO QDs were dispersed in 150 mL of ethanol. Ti_3C_2 was first added gradually under continuous stirring at room temperature, followed by the slow addition of CuO quantum dots (QDs). The suspension was stirred for 12 h and subsequently sonicated for an additional 12 h to ensure uniform dispersion. The resulting mixture was centrifuged at 4500 rpm for 10 min and washed repeatedly with deionized water until the pH of the supernatant reached ~7. Finally, the obtained precipitate was dried in a vacuum oven at 100 °C for 24 h to yield the Ti_3C_2/CuO QDs composite. The synthesis procedure is illustrated in Scheme 1.

2.5. Material characterization

To identify physical properties like crystalline phases and orientation of the powder, X-ray diffraction (XRD) using a Bruker BV 2D PHASER Best Benchtop with Cu Kα radiation was conducted, and the lattice spacing was estimated using Bragg's equation (eqn (2)):

$$n\lambda = 2d\sin\theta \quad (2)$$

where n is an integer (n = 1, 2, 3...), λ is the wavelength (Å, 1 Å = 10^{-10} m) of Cu Kα radiation (λ = 1.54 Å), d is the lattice spacing, and θ (°) is the angle of incidence (and the angle of reflection) of the X-rays with respect to the crystal planes in radians. The other XRD instrument used was a Malvern PANalytical X'Pert Pro powder diffractometer with an X'Celerator detector and variable divergence with fixed slits of Fe-filters and Co Kα radiation (λ = 1.789 Å). The Raman spectra were obtained using a WITec alpha 300 RAS+ confocal micro-Raman microscope with a laser wavelength of 532 nm and a power of less than 4.5 mW. The surface morphology was determined using a field emission scanning electron microscope (FE-SEM; Zeiss Ultra Plus 55, Japan) operated at an accelerating voltage of 2.0 kV alongside a JEOL 2100F high-resolution transmission electron microscope (HRTEM, FEI Tecnai-F30) at a 200 kV acceleration potential. The porosity properties were analyzed using N_2 adsorption/desorption isotherms using a NOVA touch NT 2LX-1 (Volts 220 USA) at 77 K, controlled using Quantachrome Touch Win Software.

2.6. Electrode preparation

For electrode preparation, the synthesized Ti_3C_2 : CuO QDs composite as the active material, acetylene black as the conductive material, and PVDF as the binder were mixed in a mortar at a percentage ratio of 80 : 10 : 10, respectively. To obtain a slurry, they were homogeneously mixed, and a suitable amount of NMP was added. The slurry was then pasted on a pre-cleaned carbon cloth current collector covering a surface of 1 cm × 1 cm^2 and oven-dried at 60 °C for 12 h. The mass loadings of Ti_3C_2 : CuO QDs composites with 1 : 0.5, 1 : 1, and 1 : 2 were 2.1 mg cm^{-2}, 3.2 mg cm^{-2}, and 3.2 mg cm^{-2}. Lastly, CuO quantum dots and pristine Ti_3C_2 were also pasted and tested alone in the same 1 M H_2SO_4 electrolyte using the same procedure to prepare electrodes with mass loadings of 3 mg cm^{-2} for CuO QDs and 3.5 mg cm^{-2} for Ti_3C_2 for individual analysis.

2.7. Electrochemical characterization

Electrochemical evaluations were all carried out at ambient temperature for 3-electrode and 2-electrode configurations using a Biologic VMP-300 potentiostat (Knoxville, TN, USA) operated using EC-Lab V11.50 software. For the 3-electrode test, Hg/Hg_2Cl_2 served as the reference electrode (RE), the prepared Ti_3C_2 : CuO QDs composite as the active electrode (working electrode, WE), and carbon glass as the counter electrode (CE). For a 2-electrode configuration, the tests were conducted using a T-plastic cell, with Whatman Celgard paper serving as a separator between the electrodes. The same procedure described in the previous section was used to prepare an asymmetric device using the Ti_3C_2 : CuO QDs composite with a mass loading of 1.1 mg cm^{-2} as the negative electrode and human hair activated carbon (HH-AC) with a

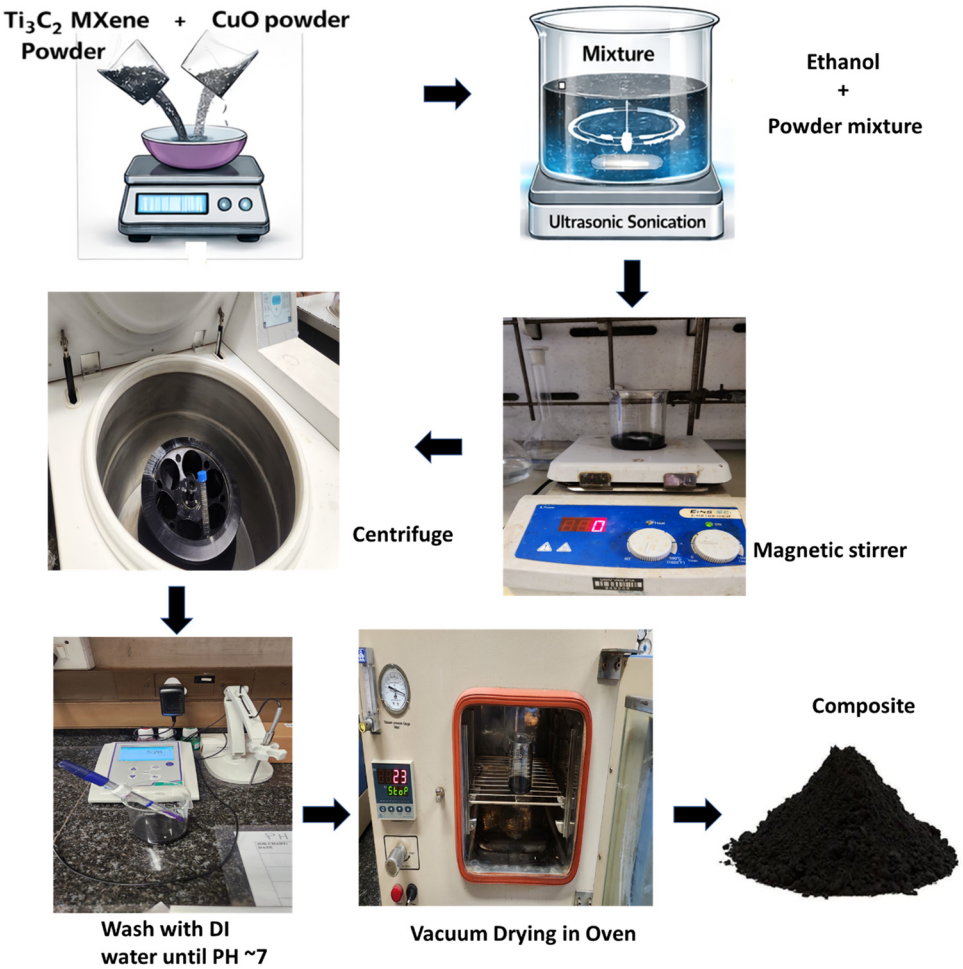

Scheme 1 Schematic diagram presenting the procedure used to synthesize the Ti_3C_2 : CuO quantum dots composites.

mass loading of 1.5 mg cm^{-2} as a positive electrode in 1 M H_2SO_4. The electrochemical evaluation was carried out using cyclic voltammetry (CV), galvanostatic charge–discharge (GCD), and electrochemical impedance spectroscopy (EIS), with EIS measurements performed over a frequency range of 100 kHz to 10 MHz at a voltage amplitude of 10 mV. The specific capacitance (C_s) was calculated from the GCD profile using eqn (3) in the 3-electrode setup and specific capacity in the 2-electrode setup using eqn (4), whereas the specific energy (E_s) and specific power (P_s) were calculated using eqn (5) and (6) depending on the type of capacitance from the GCD profile, respectively.

$$C_s\ (\mathrm{F\ g^{-1}}) = \frac{I\Delta t}{m\Delta V} \quad (3)$$

$$Q_s\ (\mathrm{mAh\ g^{-1}}) = \frac{I\Delta t}{3.6m} \quad (4)$$

$$E_s\ (\mathrm{W\ h\ kg^{-1}}) = \frac{I}{3.6(m_1+m_2)}\int V\mathrm{d}t \quad (5)$$

$$P_s\ (\mathrm{W\ kg^{-1}}) = 3600\frac{E_s}{\Delta t} \quad (6)$$

where Δt is the discharge time (s), I is the current (mA), m is the mass loaded (mg), ΔV is the potential difference (V), and dt is the discharge time integrated from the IV curve.

3. Results and discussion

3.1. Structural and morphological characterization

An *ex situ* synthesis approach was employed with the primary objective of intercalating CuO quantum dots into the interlayer space of Ti_3C_2 MXene during restacking, thereby modifying its surface and effectively passivating structural defects that could otherwise impair charge conduction and storage capability. The structural alterations induced by the incorporation of CuO QDs were investigated using Raman spectroscopy. As presented in Fig. 1(a), the characteristic peaks of pristine MXene and the Ti_3C_2 : CuO QDs composites were clearly observed. The peaks labeled ω_1, ω_2, ω_3, and ω_4 at 198, 397, 598, and 1560 cm^{-1}, respectively, were assigned to Ti_3C_2 MXene (ω_1) and the Ti_3AlC_2 MAX phase (ω_2 and ω_3), while ω_4, together with the band around 1330 cm^{-1} and 1580 cm^{-1}, corresponds to the D and G bands of amorphous carbon.[29] Additional bands observed at

265, 415, and 610 cm^{-1} are also attributed to Ti_3C_2 MXene, consistent with previously reported values.[30,31]

In the case of CuO quantum dots, distinct peaks at 282 and 616 cm^{-1} were detected, both associated with CuO vibrational modes.[32] The 282 cm^{-1} peak corresponds to the A_g vibration mode, while the 330 and 616 cm^{-1} peaks correspond to B_g vibration modes. Although a weak feature was observed at ~330 cm^{-1}, it was overshadowed by the more intense band at 282 cm^{-1}. Furthermore, a small peak around 100 cm^{-1} was observed and is attributed to Cu_2O,[33] suggesting that the synthesized CuO quantum dot powder contains minor Cu_2O impurities. The presence of trace Cu_2O may influence the electrochemical behavior, as Cu_2O possesses different electronic conductivity and redox characteristics compared to CuO. In some reports, mixed CuO/Cu_2O systems have been shown to enhance charge-transfer kinetics and provide additional redox-active sites, potentially improving pseudocapacitive performance; however, excessive Cu_2O content could reduce conductivity and structural stability. In the present work, the low intensity of the Cu_2O-related feature indicates a minor impurity level, suggesting that its influence is likely limited to subtle modifications of interfacial charge transport rather than dominating the electrochemical response.[34] Importantly, the Ti_3C_2 : CuO QDs (1 : 1) composite exhibited the characteristic peaks of both pristine MXene and CuO, confirming successful hybridization of the two components.[35,36] Similar complementary peak features were observed for the Ti_3C_2 : CuO QDs composites with ratios of 1 : 0.5 and 1 : 2, as shown in Fig. S1(a) (SI).

The observed XRD pattern of Ti_3C_2 shown in Fig. 1(b) is in close agreement with the previous study.[37] The observed diffraction angle corresponding to the (002) plane is slightly lower, but the peak is very sharp and intense, and higher-order peaks are ascribed to the restacking of $Ti_3C_2T_x$ flakes.[38] The peak also symbolizes the high crystallinity of the material, which is expected to enhance electronic conductivity and facilitate efficient charge transport during electrochemical processes. The diminished peak observed at the Miller index (104) in the XRD pattern corresponds to the partial removal of the Al layer from Ti_3AlC_2 (which corresponds to JCPDS card no. 52-0875)[39] during the etching process, indicating the successful formation of Ti_3C_2 MXene, a structural transformation that increases interlayer spacing and promotes improved electrolyte ion accessibility. The diffractogram intensity scale was adjusted to better visualize the weaker peaks that appeared after etching.

The typical XRD pattern of CuO quantum dots (QDs) is presented in Fig. 1(b), showing diffraction peaks at 2θ values corresponding to the (110), (111), (020), (202), and (311) planes, characteristic of monoclinic CuO (corresponding to JCPDS No. 48-1548).[40,41] XRD measurements of pristine Ti_3C_2 and CuO were performed using a Bruker BV 2D PHASER diffractometer equipped with Cu Kα radiation. In contrast, the Ti_3C_2 : CuO QDs (1 : 1) composite was analyzed using a Malvern PANalytical X'Pert Pro powder diffractometer with Co Kα radiation, which resulted in a slight shift of diffraction peaks toward higher 2θ values compared to those obtained with Cu Kα radiation, suggesting possible lattice interaction and interfacial coupling between Ti_3C_2 layers and CuO quantum dots, which may contribute to improve charge transfer behavior.

The XRD patterns confirmed that all Ti_3C_2 : CuO QDs composites with mass ratios of 1 : 0.5, 1 : 1, and 1 : 2 were successfully synthesized, as the characteristic peaks of both pristine Ti_3C_2 and CuO are evident from Fig. 1(b) and Fig. S1(b). The average crystallite size of the CuO QDs, calculated using the Scherrer equation, was approximately 7.5 nm – consistent with the typical size range of quantum dots (2–10 nm). Such nanoscale crystallite dimensions increase surface-active sites and shorten ion diffusion pathways, which are beneficial for enhancing electrochemical kinetics and capacitive performance. The Scherrer equation used for this calculation is given in eqn (7):[42]

$$D = \frac{K\lambda}{\beta \cos\theta} \tag{7}$$

where D is the crystallite size (nm), K is the Scherrer constant (dimensionless shape factor), λ is the wavelength of X-ray radiation used, β is the full width at half maximum (FWHM)

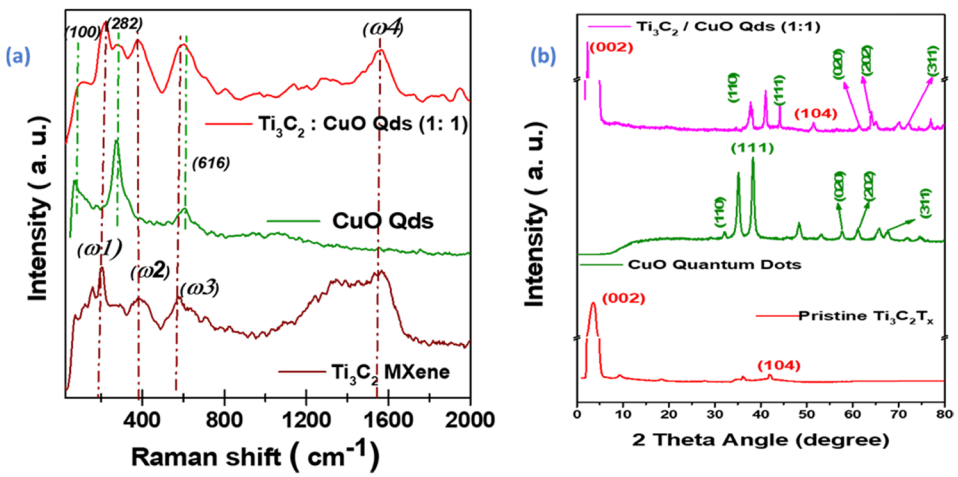

Fig. 1 (a) Raman spectra and (b) XRD patterns of the prepared Ti_3C_2, CuO quantum dots and the Ti_3C_2 : CuO QDs (1 : 1) composite.

of the diffraction peak in radians, and θ is the Bragg angle (or diffraction angle).

The surface morphology of both pristine Ti_3C_2 MXene and CuO quantum dots was examined using a scanning electron microscope (SEM), as shown in Fig. 2(a, b) and (c, d), under different magnifications. The pristine Ti_3C_2 MXene appears multilayered with gaps between the layers to accommodate ion transport, which is beneficial for facilitating electrolyte diffusion and reducing ion transport resistance during electrochemical cycling, whereas CuO quantum dots appear spindle/rod-shaped and agglomerated or grouped, forming clumps, providing additional electrochemically active sites associated with pseudocapacitive redox reactions. The second method for determining the size of CuO quantum dots involved using the SEM image and ImageJ software. The ImageJ software measured different quantum dots and different sizes and plotted them as histogram, in which the Gaussian distribution function was implemented to determine the particle size which was found to be 2.09 nm; a nanoscale dimension expected to enhance surface-to-volume ratio and improve charge-transfer kinetics. Fig. 2(e and f) shows the Ti_3C_2 : CuO QDs composite with a 1 : 1 ratio, with quantum dots inserted between the layers of MXene, and some glued to the surface of the layers, indicating strong interfacial contact that may promote efficient electron transport pathways between conductive MXene sheets and electroactive CuO quantum dots. Fig. S2(a and b) (SI) shows the as-synthesized Ti_3AlC_2 MAX phase with layers closely stacked before HF etching; successful etching and exfoliation are evident in Fig. 2(a and b), which displays separated Ti_3C_2 layers, a structural modification known to increase accessible surface area and enhance electrochemical performance. Examination of the Ti_3C_2 : CuO QDs composites reveals a clear dependence of quantum dot (QD) distribution on the Ti_3C_2 : CuO mass ratio.

At a ratio of 1 : 0.5 (Fig. S2(c and d)), CuO QDs are sparsely distributed and appear isolated on the MXene surface and between layers, indicating limited surface coverage, which may result in fewer active redox sites and lower overall capacitance contribution. At a 1 : 1 ratio (Fig. 2(e and f)), QDs are more uniformly distributed both on the surface and in the interlayer regions of Ti_3C_2, producing an even coverage that maximizes accessible active sites without severely hindering ion transport, thereby supporting enhanced electrochemical kinetics and reduced charge-transfer resistance. By contrast, at a 1 : 2 ratio (Fig. S2(e and f)), the QDs exhibit pronounced aggregation and apparent over-coverage; this excessive loading can obstruct electrolyte ingress to internal active sites and may therefore reduce effective utilization of the electrode material, potentially

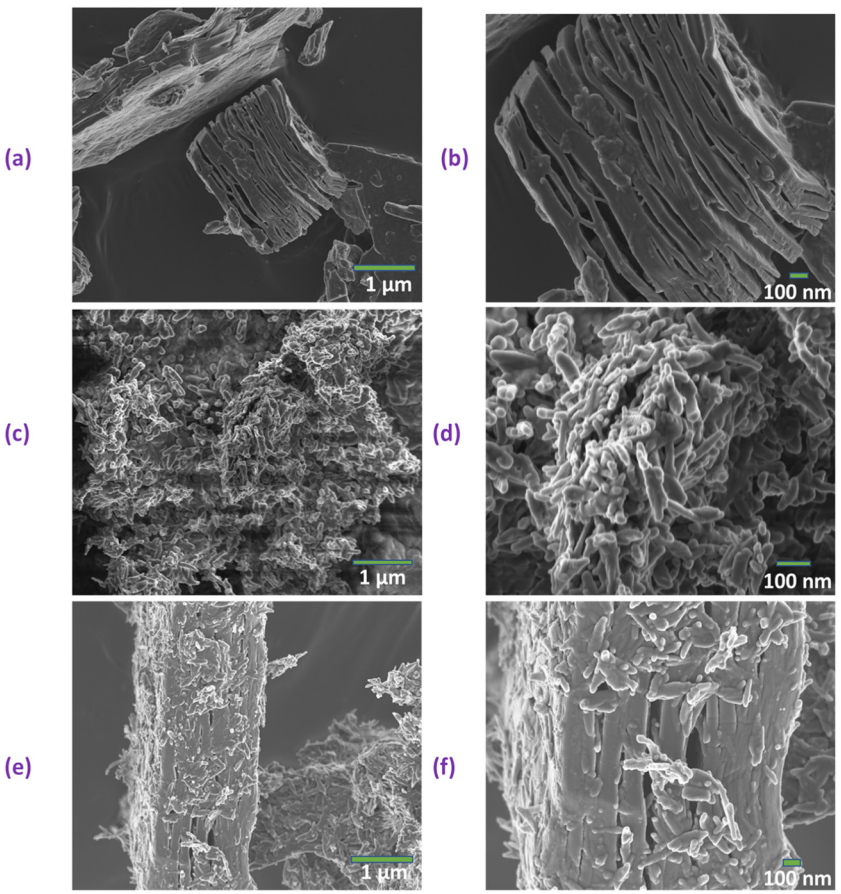

Fig. 2 SEM images of (a and b) $Ti_3C_2T_x$ MXene, (c and d) CuO quantum dots (QDs), and (e and f) Ti_3C_2 : CuO QDs (1 : 1) at low and high magnifications, respectively.

increasing diffusion resistance and limiting rate capability. Collectively, these morphological observations suggest that the 1 : 1 composite provides the best compromise between active-site availability and ion accessibility, whereas underloading (1 : 0.5) limits the available pseudocapacitive material and overloading (1 : 2) risks impeding electrolyte transport, highlighting a clear structure–property relationship between morphology, ion accessibility, and electrochemical performance.

Transmission electron microscopy (TEM) analysis was performed to investigate the morphology and structural characteristics of Ti_3C_2 MXene and the MXene–CuO quantum dot composite (Fig. 3(a and b)). The pristine MXene (Fig. 3(a)) exhibits typical layered and accordion-like nanosheet morphology with thin, stacked lamellae, confirming successful exfoliation of the MAX precursor into two-dimensional Ti_3C_2 sheets. The transparent and wrinkled nature of the layers suggests few-layer structures with high surface area, which is consistent with previously reported MXene morphologies.[35] Upon incorporation of CuO quantum dots (Fig. 3(b)), the MXene sheets retain their layered framework while exhibiting darker contrast regions attributed to the deposition of nanoscale CuO particles on the MXene surface. The homogeneous distribution of these nanostructures indicates strong interfacial interaction between MXene and CuO, which is expected to enhance electron transport pathways and prevent restacking of the nanosheets. The preservation of sheet-like morphology alongside nanoparticle decoration confirms successful formation of the hybrid architecture, supporting improved electrochemical behavior through synergistic coupling between conductive MXene layers and electroactive quantum dots. Similar morphological evolution has been reported for MXene-based hybrid nanostructures designed for energy storage applications.[35]

The TEM analysis was conducted to evaluate the morphology and size distribution of the CuO quantum dots and pristine CuO structures (Fig. 3(c–e)). The high-magnification image (Fig. 3(c)) reveals uniformly dispersed nanoscale quantum dots with well-defined boundaries, confirming the successful synthesis of nanosized CuO particles.[34] Statistical analysis based on 98 counted particles (Fig. 3(e)) indicates a narrow size distribution with particle diameters ranging from 1.44 to 10.81 nm and a standard deviation of 1.72 nm, demonstrating good size uniformity typical of quantum dot systems. The small particle size is expected to enhance surface area and increase the density of electrochemically active sites, which is beneficial for charge storage applications. In contrast, the TEM image of pure CuO (Fig. 3(d)) shows larger aggregated structures with elongated morphology, highlighting the significant reduction in particle size achieved in the quantum dot form. This nanoscale confinement is anticipated to improve electron transport kinetics and facilitate faster ion diffusion compared to bulk CuO structures.[34]

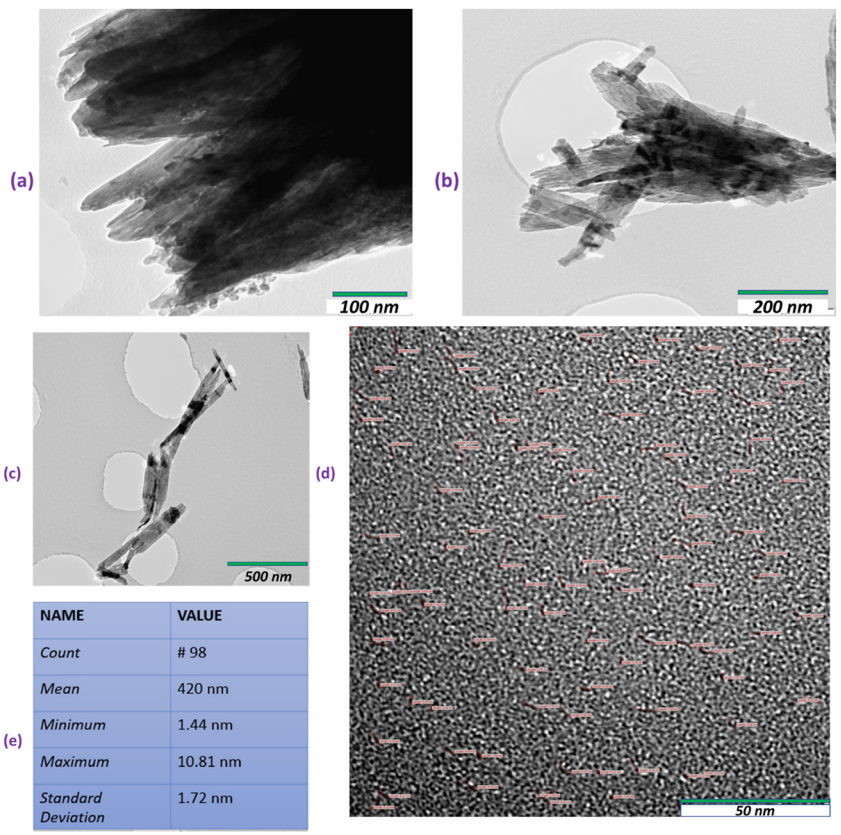

NAME	VALUE
Count	# 98
Mean	420 nm
Minimum	1.44 nm
Maximum	10.81 nm
Standard Deviation	1.72 nm

Fig. 3 TEM images of (a) $Ti_3C_2T_x$ MXene, (b) Ti_3C_2 : CuO QDs (1 : 1), (c and d) CuO quantum dots (QDs) at different magnifications, and (e) statistical table for CuO QDs.

Energy-dispersive X-ray spectroscopy (EDS) elemental mapping and spectra (Fig. 4(a–f)) were used to confirm the elemental composition and spatial distribution of the synthesized Ti_3C_2 MXene, CuO quantum dots, and their composite structure. The layered morphology observed in Fig. 4(a) is characteristic of exfoliated MXene sheets, while the corresponding EDS spectrum (Fig. 4(b)) shows dominant Ti (17.9%) and C (43.6%) peaks along with O (14.1%) and F (22.4%) signals attributed to surface terminations (–O, –OH, –F) commonly formed during chemical etching of MAX phases.[35] The lower atomic percentage of Al (1.9%) might originate from the substrate plate that holds the sample, and additionally the imbalance in the atomic ratios is caused by ethanol (C_2H_5OH) that was used to prepare samples, adding more carbon and oxygen. CuO quantum dots exhibit a more granular morphology (Fig. 4(c)), and the EDS spectrum (Fig. 4(d)) confirms the presence of strong Cu (56.6%) and O (41.9%) peaks, indicating successful formation of copper oxide nanoparticles. In the composite sample (Fig. 4(e)), simultaneous detection and uniform distributions of Ti (13.4%), C (43.1%), Cu (6.4%), F (13.4%), and O (22.2%) demonstrate successful hybridization of CuO quantum dots onto the MXene surface, suggesting strong interfacial interaction and effective dispersion.[36] Such homogeneous elemental distribution is known to enhance interfacial electron transport and improve electrochemical performance by facilitating charge transfer between conductive MXene sheets and active metal oxide nanoparticles.[35] These observations are consistent with previously reported MXene-based hybrid nanostructures, where EDS analysis confirms compositional integration and surface functionalization effects.[36]

The Brunauer–Emmett–Teller (BET) method was used to measure the N_2 adsorption/desorption isotherms, which are shown in Fig. 5(a). They assist in understanding the pore structure and surface area of the materials, which directly influence electrolyte accessibility, ion diffusion pathways, and electrochemical performance. Pristine MXene shows a very low adsorption volume at low relative pressures, indicating a non-porous or low-porosity structure with minimal surface area, a feature that may limit active surface exposure and reduce capacitance contribution. The isotherm exhibits a type III shape with an H3 hysteresis loop,[42] which is characteristic of non-porous or plate-like particles forming slit-shaped mesopores with weak adsorbate–adsorbent interaction, consistent with restacked layered structures that can restrict ion transport channels. The pristine MXene has a surface area of 3.46 $m^2 g^{-1}$, which is relatively small due to the restacking of the layers of MXene, but relatively close to other works.[43,44] It was slightly improved in other works when layers of MXene were intercalated or delaminated,[43,44] highlighting the importance of structural modification in enhancing electrochemical accessibility.

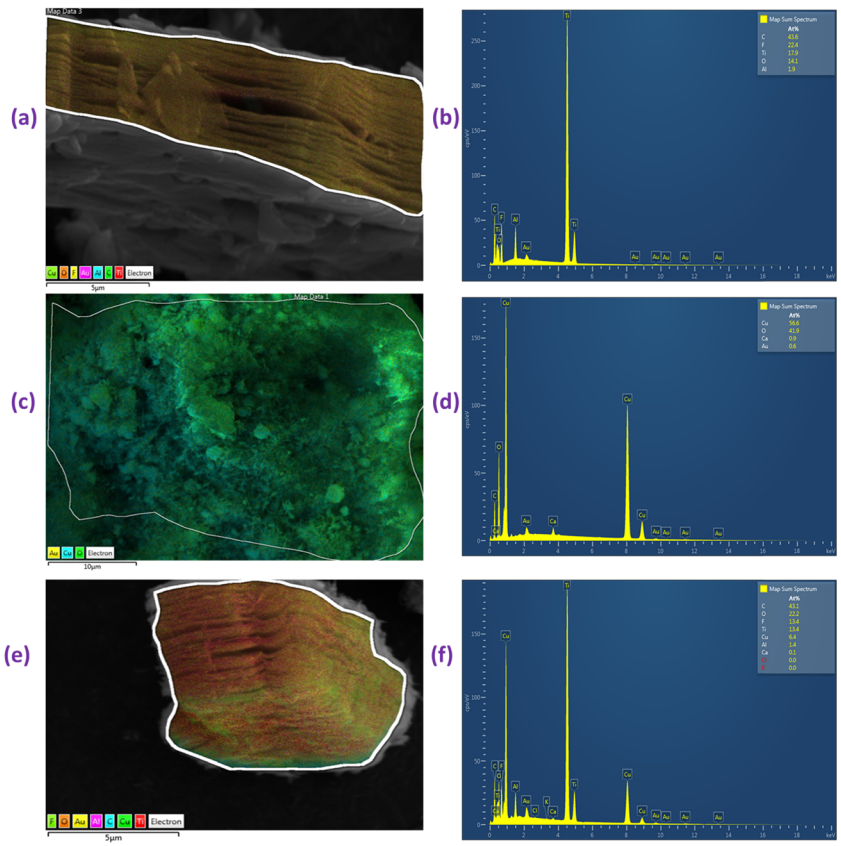

Fig. 4 Energy-dispersive X-ray spectroscopy (EDS) images and spectra of (a and b) $Ti_3C_2T_x$ MXene, (c and d) CuO quantum dots (QDs), and (e and f) Ti_3C_2 : CuO QDs (1 : 1), respectively.

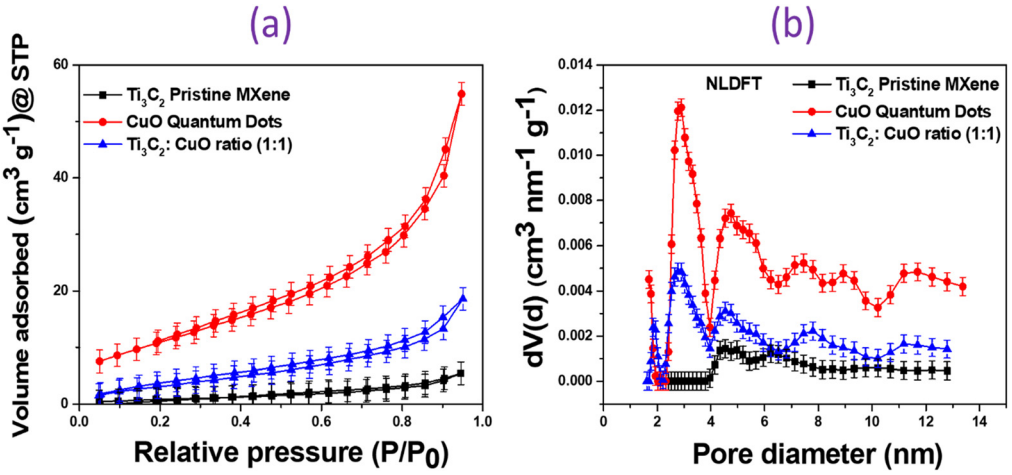

Fig. 5 (a) N_2 adsorption/desorption isotherms and (b) PSD calculated using NLDFT.

The CuO quantum dots have the highest adsorption volume with relative pressure, but adsorption gradually increases in the low relative pressure region, suggesting the presence of mesopores, which can facilitate electrolyte penetration and increase electrochemically active surface area. A sharp increase at high relative pressure ($P/P_0 > 0.9$) might be indicative of capillary condensation in larger mesopores or macropores. The curve resembles a type 4 isotherm with H3-type hysteresis,[44,45] and it contains a surface area of 39.6 $m^2\ g^{-1}$. It is noticed that the addition of CuO quantum dots to Ti_3C_2 MXene (Fig. 5(a) and Fig. S3(a)) increases the adsorption volume at low relative pressures and the area of the surface of interaction increases to 17.4 $m^2\ g^{-1}$, 17.9 $m^2\ g^{-1}$ and 25.7 $m^2\ g^{-1}$ for the composite ratios of 1 : 1, 1 : 0.5 and 1 : 2, respectively, which suggests partial enhancement of surface area and porosity due to CuO incorporation, thereby potentially improving ion diffusion kinetics and charge storage capability. To obtain more information to support these results, pore size distribution (PSD) was calculated using non-local density functional theory (NLDFT).

From Fig. 5(b) and Fig. S3(b), pristine MXene shows a very low pore volume across all diameters. Small peaks around the mesoporous region and a flat baseline in the microporous region suggest the absence of significant macropores, which may contribute to limited electrolyte-accessible active sites. As for CuO, it shows multiple peaks, with the most intense peak occurring between 2 and 4 nm, corresponding to the mesoporous region. Additional peaks observed in the 4–13 nm range indicate a broad distribution of mesopores, supporting improved ion transport and electrolyte diffusion. In the microporous region (<2 nm), smaller peaks are also present, confirming the existence of micropores; however, they are less dominant compared to mesopores. For composites with 1 : 0.5, 1 : 1, and 1 : 2 ratios, introducing quantum dots increases the surface area relative to pristine MXene by preventing complete restacking of MXene sheets by occupying interlayer spaces and adhering to the MXene surface, thereby creating additional accessible sites and exposing more active surface area for electrolyte interaction,[46–49] which is expected to reduce diffusion resistance and enhance electrochemical kinetics.

However, the overall pore volume is lower than that of pure CuO due to partial blocking of pores when CuO attaches to the MXene surface or fills MXene interlayer gaps, indicating a balance between increased conductivity from MXene and porosity from CuO, which governs overall electrochemical behavior. The shift and broadening of pore size distribution in the composite indicate a synergistic structural modification, potentially improving ion transport in electrochemical applications, consistent with enhanced charge transfer and improved electrode performance observed electrochemically. The above observation is evidenced by both Fig. 5(b) and Fig. S3(b).

3.2. Electrochemical characterization

3.2.1. Three-electrode system. The electrochemical properties of pristine Ti_3C_2 MXene, CuO quantum dots (QDs), and their composites (Ti_3C_2 : CuO = 1 : 0.5, 1 : 1, and 1 : 2) were systematically investigated using cyclic voltammetry (CV), galvanostatic charge–discharge (GCD), and electrochemical impedance spectroscopy (EIS), as shown in Fig. S6 (SI), where a detailed comparison of all composites with different ratios is presented. Based on this comparative analysis, the 1 : 1 Ti_3C_2 : CuO composition exhibited the most favorable electrochemical performance and was therefore selected as the optimized composite for detailed discussion. All measurements were performed within a potential window of 0.0 to −0.5 V at a scan rate of 20 mV s^{-1} in 1 M H_2SO_4.

The CV curves in Fig. 6(a) display quasi-rectangular profiles characteristic of electric double-layer capacitive (EDLC) behavior. Among the tested electrodes, the Ti_3C_2 : CuO QDs (1 : 1) composite exhibits the largest enclosed area, indicating enhanced charge storage capability resulting from the synergistic interaction between the conductive Ti_3C_2 layers and the pseudocapacitive CuO domains. Correspondingly, the GCD curves in Fig. 6(b) show nearly symmetric triangular shapes, confirming good capacitive reversibility. The composite electrode also delivers a noticeably longer discharge time than

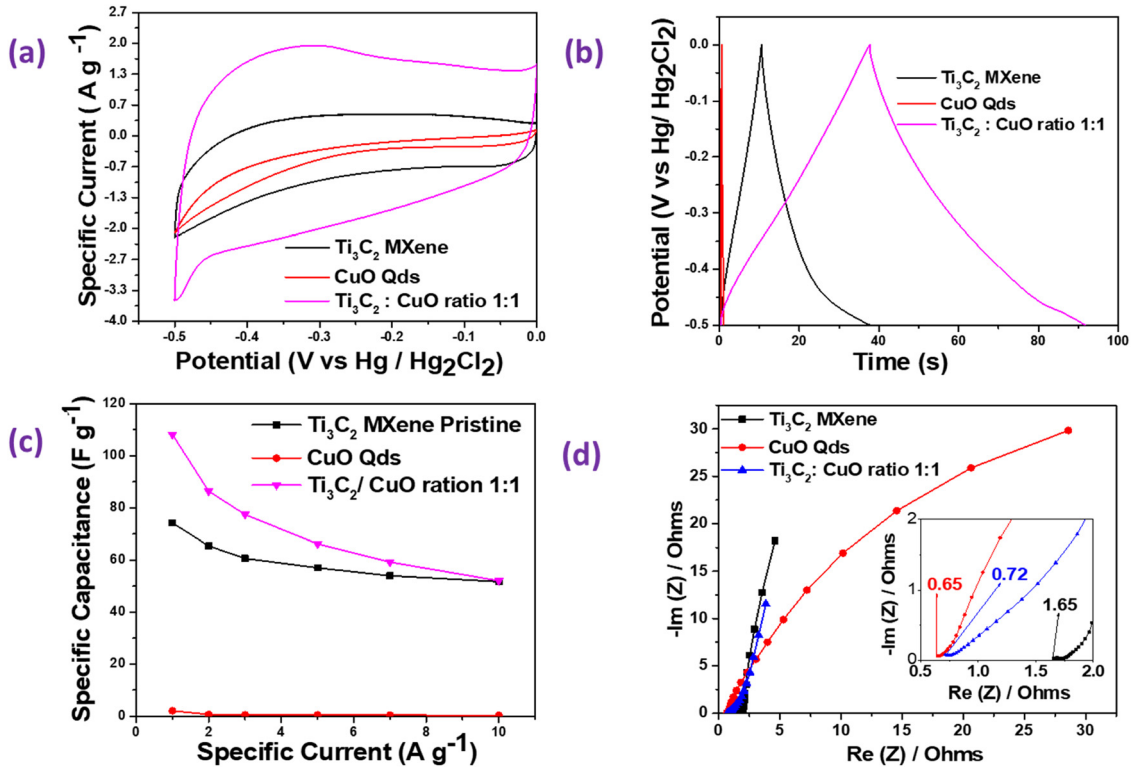

Fig. 6 (a) CV curves of the Ti_3C_2 MXene, CuO quantum dots and the Ti_3C_2 : CuO QDs (1 : 1) composite recorded at 20 mV s^{-1}; (b) GCD curves of the Ti_3C_2 MXene, CuO quantum dots and the Ti_3C_2 : CuO QDs (1 : 1) composite recorded at 1 A g^{-1}; (c) specific capacitance *vs.* specific current for all three materials and (d) comparison of the EIS Nyquist plots of Ti_3C_2, CuO and Ti_3C_2 : CuO QDs with an enlarged high-frequency region shown as an inset.

either pristine Ti_3C_2 or CuO, reflecting its superior energy storage efficiency.

The specific capacitances calculated from GCD data (Fig. 6(c)) further highlight the excellent performance of the Ti_3C_2 : CuO (1 : 1) electrode, which achieves a value of 108.1 F g^{-1}, surpassing those of pristine Ti_3C_2 (74.2 F g^{-1}), CuO QDs (2.2 F g^{-1}), the 1 : 0.5 composite (89.2 F g^{-1}) and the 1 : 2 composite (76.6 F g^{-1}). The enhanced capacitance at a 1 : 1 ratio is attributed to the optimal integration of Ti_3C_2's high conductivity with CuO's abundant redox-active sites. Although the 1 : 2 composite exhibits the highest specific surface area, a larger SSA does not necessarily guarantee superior electrochemical performance. The excessive CuO loading may increase surface area, but it can also promote aggregation, partial pore blockage, and reduced electrical conductivity, thereby limiting efficient charge transfer and ion transport. Consequently, the 1 : 1 composite provides a more balanced combination of accessible active sites and conductive pathways, leading to improved overall performance.

The Nyquist plot in Fig. 6(d) provides further insight into the interfacial charge dynamics. The composite electrode exhibits a lower equivalent series resistance (0.72 Ω) than pristine Ti_3C_2 (1.65 Ω), consistent with the improved conductivity facilitated by CuO, which possesses an intrinsically low ESR (0.65 Ω). The steeper slope in the low-frequency region also indicates enhanced ion diffusion and capacitive behavior.

Taken together, the structural, morphological, and electrochemical analyses collectively demonstrate that the Ti_3C_2 : CuO hybrid effectively overcomes the intrinsic limitations of pristine Ti_3C_2 (such as layer restacking and limited porosity) and CuO (notably low electrical conductivity). SEM and TEM observations confirm the successful incorporation and uniform distribution of CuO quantum dots into and on the surface of the Ti_3C_2 layers, which helps prevent severe restacking and creates a more open and accessible architecture. BET surface area and pore size distribution analyses further reveal the development of a hierarchical structure with enhanced ion-accessible surface area as compared to pristine Ti_3C_2, facilitating improved electrolyte diffusion and active site exposure. These physicochemical characteristics directly translate into enhanced electrochemical behavior, as evidenced by improved charge transfer kinetics and capacitive response. The synergistic integration of conductive pathways from Ti_3C_2 and redox-active sites from CuO[49] results in a composite that delivers superior capacitance, reversibility, and rate capability. Overall, the strong correlation between the engineered microstructure and electrochemical performance establishes Ti_3C_2 : CuO QDs composites as promising electrode materials for high-performance supercapacitors. The electrochemical impedance spectroscopy (EIS) analysis in Fig. 6(d) revealed a negligible charge transfer resistance (R_{ct}), indicating highly efficient electron transport across the electrode–electrolyte interface. The absence of a distinct semicircle in the high-frequency region suggests that the interfacial charge transfer process is not kinetically limited, which can be attributed to the intrinsic high conductivity of Ti_3C_2 MXene and the intimate interfacial contact

with CuO quantum dots. Rather than indicating weak interaction, the R_{ct}, which was negligibly small, supports the formation of a well-integrated hybrid structure (with a composite ratio of 1 : 1) that facilitates rapid charge transfer.

Electrochemical impedance spectroscopy (EIS) analysis was performed, and the corresponding fitting results are presented in Fig. 7(a–c), where the equivalent circuit model and the extracted EIS curves from the fitting and experimental results are shown. The impedance spectra were fitted using an equivalent circuit comprising solution resistance (R_s = $R1$), charge-transfer resistance (R_{ct} = $R3$), constant-phase elements (CPEs, $Q2$ and $Q3$), and an additional interfacial resistive element ($R2$) to account for electrode porosity and interfacial inhomogeneity. The Nyquist plots exhibit a small high-frequency intercept on the real axis corresponding to the equivalent series resistance (ESR). Comparison between the experimentally observed ESR (from the high-frequency intercept) and the fitted R_s values (see the values in the figure) shows good agreement for all three electrodes, confirming the validity of the selected equivalent circuit. Among the samples, the composite electrode shows a much lower ESR (as compared to pristine MXene), indicating improved electronic conductivity and reduced internal resistance due to the synergistic interaction between MXene and CuO quantum dots. The use of the same equivalent circuit for all samples indicates that they follow the same basic electrochemical process. However, the differences in the fitted parameters show that the composite has faster charge transfer and improved interfacial properties compared to the pristine materials. The electrochemical behavior of the Ti_3C_2 : CuO QDs (1 : 1) composite was systematically studied through CV, GCD, and long-term cycling stability tests, as shown in Fig. 8(a–c). The CV curves recorded at scan rates ranging from 5 to 100 mV s^{-1} in Fig. 8(a) exhibit nearly symmetric and quasi-rectangular shapes, characteristic of ideal capacitive behavior. At higher scan rates, the CV profiles retained their shape without significant distortion, suggesting excellent rate capability and rapid ion transport within the electrode. This behavior demonstrates that the hierarchical pore architecture and the synergistic contribution of Ti_3C_2 conductivity with CuO redox activity effectively facilitate fast charge storage dynamics.

The GCD profiles obtained at various current densities from 1 to 10 A g^{-1}, as shown in Fig. 8(b), revealed well-defined triangular shapes with nearly linear charge and discharge slopes, further confirming good capacitive reversibility. Importantly, the composite electrode exhibited long discharge durations at low current densities (*i.e.*, 1 A g^{-1}), indicative of its high charge storage capacity. Even at high current densities (10 A g^{-1}), the curves remained symmetric, reflecting stable electrochemical performance and efficient electron/ion transport pathways.

The cycling stability of the composite was further examined at a constant current density of 5 A g^{-1} over 5000 continuous charge–discharge cycles in Fig. 8(c). The Ti_3C_2 : CuO electrode retained 90.9% of its initial capacitance, demonstrating excellent long-term durability. Additionally, the coulombic efficiency remained close to 100% throughout the entire cycling process, confirming highly reversible charge–discharge processes and stable electrode–electrolyte interactions. Such durability

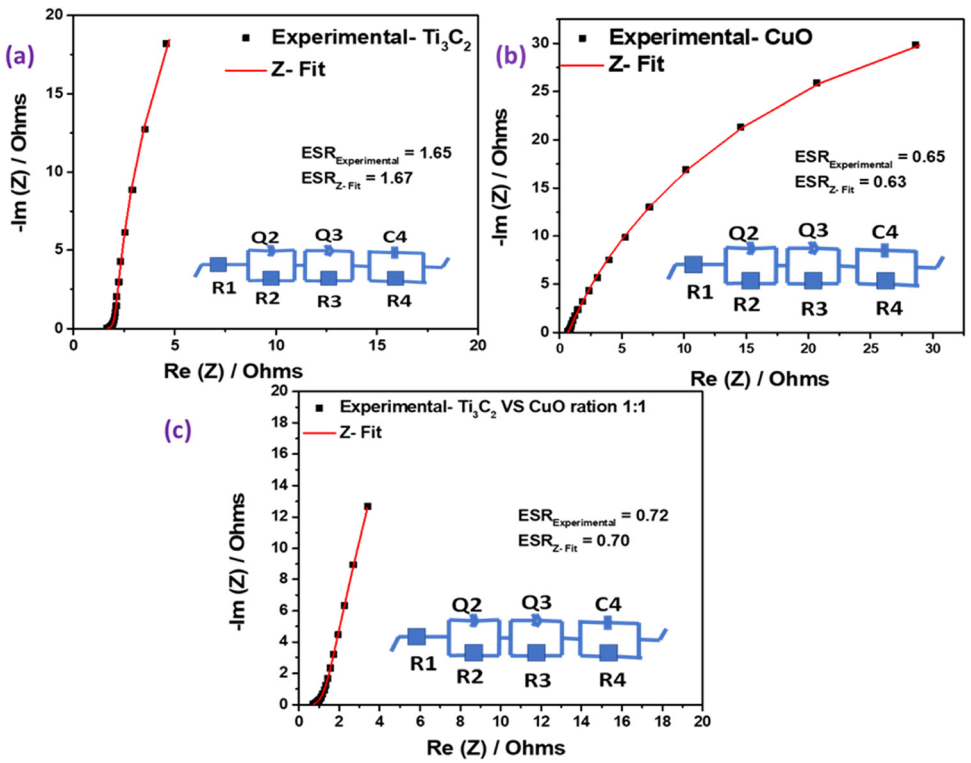

Fig. 7 The fitted EIS Nyquist plot for (a) Ti_3C_2 MXene, (b) CuO QDs, and (c) the Ti_3C_2 : CuO QDs (1 : 1) composite.

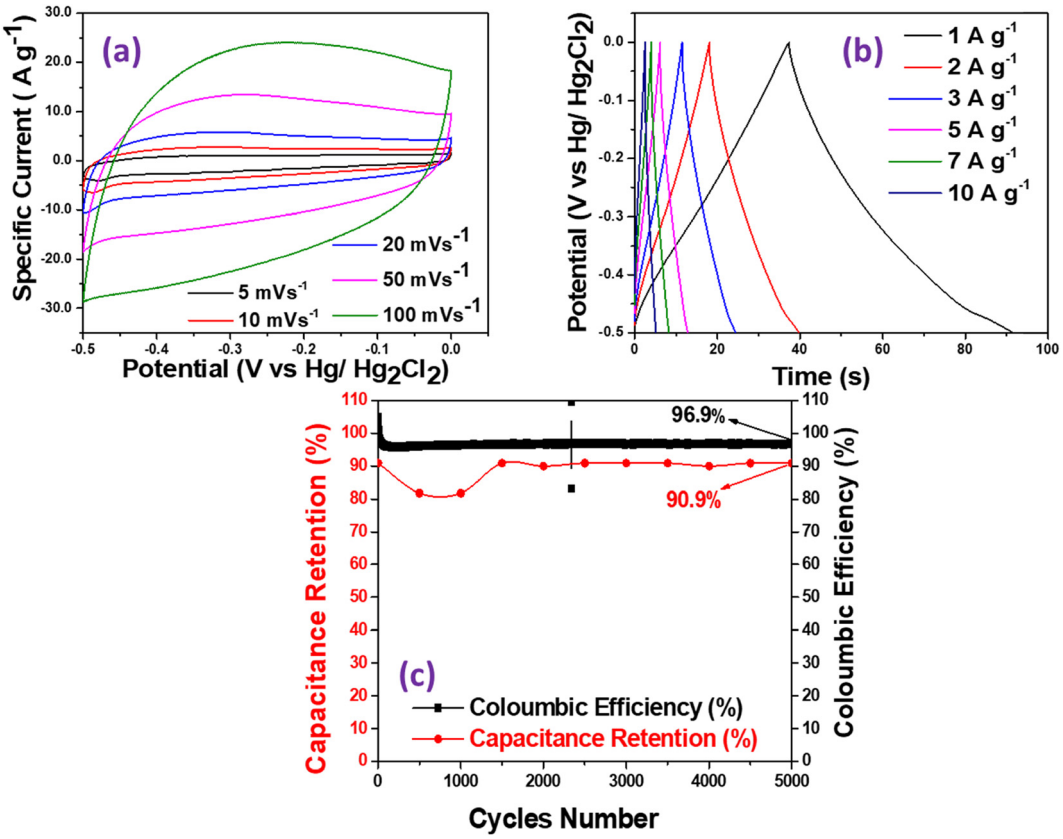

Fig. 8 (a) Full CV scan of the optimal Ti_3C_2 : CuO QDs (1 : 1) composite at different scan rates, (b) GCD scan of the Ti_3C_2 : CuO QDs (1 : 1) composite at different specific currents, and (c) cycling performance of the Ti_3C_2 : CuO QDs (1 : 1) composite over 5000 cycles at 5 A g^{-1}.

highlights the robust structural stability imparted by CuO nanoparticles, which prevent MXene restacking while providing additional redox-active sites for charge storage. In summary, the Ti_3C_2 : CuO QDs composite delivers a combination of high-rate capability, remarkable cycling stability, and excellent coulombic efficiency.

Trasatti's method was used to determine non-diffusion (capacitive) and diffusion-controlled contributions of MXene and its CuO QDs (1 : 1) composite. Fig. 9(a and f) summarize the kinetic and charge-storage behavior of pristine Ti_3C_2 and the Ti_3C_2 : CuO quantum dot (1 : 1) composite derived from cyclic voltammetry analysis. In Fig. 9(a), the log(i)–log(v) relationship shows higher b-values for the composite ($b \approx 0.76$) than for pristine Ti_3C_2 ($b \approx 0.62$), indicating a stronger surface-controlled (capacitive) contribution after CuO QD incorporation. Fig. 9(b) and (c), based on the Trasatti method, separate total capacitance into outer (surface-controlled) and inner (diffusion-controlled) components,[50] revealing that the composite exhibits both higher total capacitance and lower diffusion resistance compared to Ti_3C_2. This might be due to increased exposure of the MXene surface after layers were opened by CuO intercalation. Fig. 9(d) quantitatively confirms this trend, showing an increased capacitive contribution (56%) for Ti_3C_2 : CuO QDs relative to pristine Ti_3C_2 (46%). The shaded CV profiles in Fig. 9(e) and (f) further illustrate that CuO QD decoration enlarges the capacitive current region while maintaining diffusion-assisted charge storage, highlighting synergistic pseudocapacitive and intercalation processes.[50] Overall, the results demonstrate that coupling CuO quantum dots with MXene enhances charge-transfer kinetics and optimizes the balance between capacitive and diffusion-controlled storage, thereby improving electrochemical performance.

3.3. Two-electrode systems

To further evaluate the practical applicability of the Ti_3C_2 : CuO QDs composite, an asymmetric supercapacitor (ASC) device was assembled using Ti_3C_2 : CuO (1 : 1) as the negative electrode and human hair-derived activated carbon (HH-AC) as the positive electrode in 1 M H_2SO_4, where the human hair-derived activated carbon (HH-AC) was synthesized *via* chemical activation using KOH. The material exhibited a highly porous micro/mesoporous structure with a high BET surface area of 3429 m^2 g^{-1} as further displayed by the BET plot in Fig. S7. Its electrochemical testing in 1 M H_2SO_4 delivered a specific capacitance of 107.1 F g^{-1} at 1 A g^{-1} within a 0.7 V potential window, while measurements in 2.5 M KNO_3 showed excellent cycling stability with 97% capacitance retention after 10 000 cycles.[27] The HH-AC was extensively studied in our previous work.[27] The electrochemical performance of the device was systematically characterized through cyclic voltammetry (CV), galvanostatic charge–discharge (GCD), specific capacity analysis, and electrochemical impedance spectroscopy (EIS), as

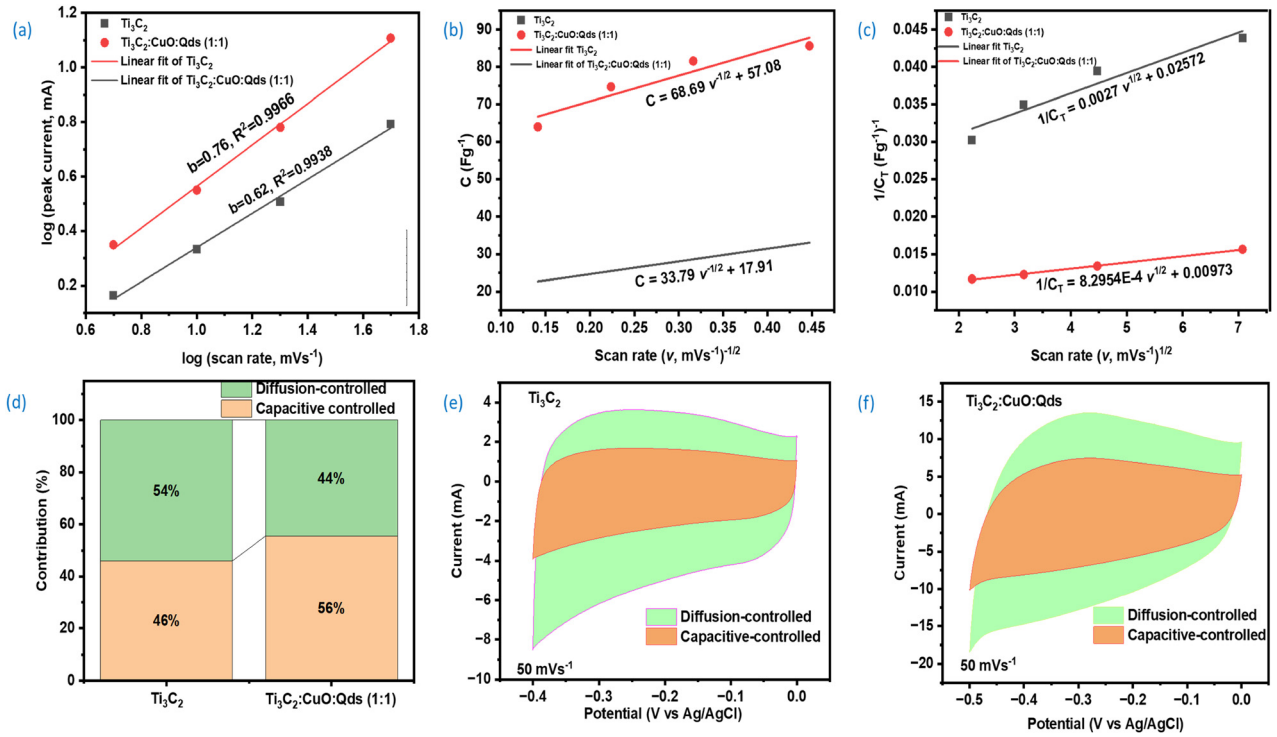

Fig. 9 Trasatti's method for differentiating diffusion and non-diffusion contributions: (a) log(i) as a function of log(ν); (b) capacitance as a function of the reciprocal square root of scan rate; (c) plot of inverse total capacitance ($1/C_t$) *versus* $\nu^{1/2}$; (d) percentage comparison of capacitive-controlled and diffusion-controlled contributions for Ti_3C_2 and Ti_3C_2 : CuO QDs (1 : 1); (e) capacitive (orange) and diffusion-controlled (green) current contributions extracted from the CV curves of pristine Ti_3C_2 at 50 mV s^{-1} and (f) the corresponding capacitive and diffusion-controlled current separation for the Ti_3C_2 : CuO QDs (1 : 1) composite at 50 mV s^{-1}.

shown in Fig. 10(a–e). Since the materials perform differently at positive and negative potentials, charge balancing was carried out to adjust the amount of mass loading in both electrodes of the device using eqn (8):

$$\frac{m_+}{m_-} = \frac{C_{s-} \cdot \Delta V_-}{C_{s+} \cdot \Delta V_+} \quad (8)$$

where m_+ and m_- are the positive and negative masses of the active electrode, and C_{s+}, C_{s-}, V_+, and V_- are the specific capacitances and potential differences for the positive and negative electrodes, respectively. According to eqn (8), m_+ and m_- were estimated to be 1.1 mg cm^{-2} and 1.5 mg cm^{-2}; therefore, the total mass is 2.6 mg cm^{-2}.

The CV curves in Fig. 10(a) show the comparative CV curves of the composite (1 : 1) and HH-AC at 20 mV s^{-1} before being assembled into a device. The curves are rectangular-shaped, but when assembled into a symmetric device (Ti_3C_2/CuO//HH-AC) shown in Fig. 10(b), the device exhibits quasi-rectangular CV profiles with distinct redox humps, indicating an overall pseudocapacitive behavior. Furthermore, the CV curves at increasing scan rates from 5 to 500 mV s^{-1} in Fig. 10(b) retained their shapes with only slight distortion at higher rates, suggesting excellent rate capability and rapid charge-transfer kinetics. This behavior confirms that the hierarchical pore structure of HH-AC ensures efficient ion adsorption, while the composite electrode provides fast electron transport and redox-active sites. The GCD measurements in Fig. 10(c) further validated the device's performance. Nearly triangular and symmetric charge–discharge curves were obtained at current densities ranging from 1 to 10 A g^{-1}, confirming good electrochemical reversibility. Notably, the device maintained a long discharge time at low specific current (1 A g^{-1}), indicative of high specific capacity. With increasing specific currents, the discharge time gradually decreased, yet the curves remained symmetric, demonstrating excellent structural and electrochemical stability during fast charge–discharge cycling.

The specific capacity values of the Ti_3C_2 : CuO//HH-AC device are plotted in Fig. 10(d). At 1 A g^{-1}, the device delivered a specific capacity of 13.3 mAh g^{-1}, and although the capacity decreased with increasing specific current, it retained 33.4% of its initial capacity at 10 A g^{-1}. This performance is attributed to the complementary functions of the electrodes: the high surface area and conductivity of HH-AC provide efficient double-layer charge storage, while Ti_3C_2 : CuO contributes faradaic charge storage and enhances overall conductivity.

Electrochemical impedance spectroscopy (EIS) was conducted to evaluate the charge-transfer and ion-transport characteristics of the device, as shown in Fig. 10(e). Measurements were performed over a frequency range of 100 kHz to 10 MHz with a voltage amplitude of 10 mV. The resulting Nyquist plot exhibits a small intercept on the real axis at high frequency, corresponding to an equivalent series resistance (R_s) of

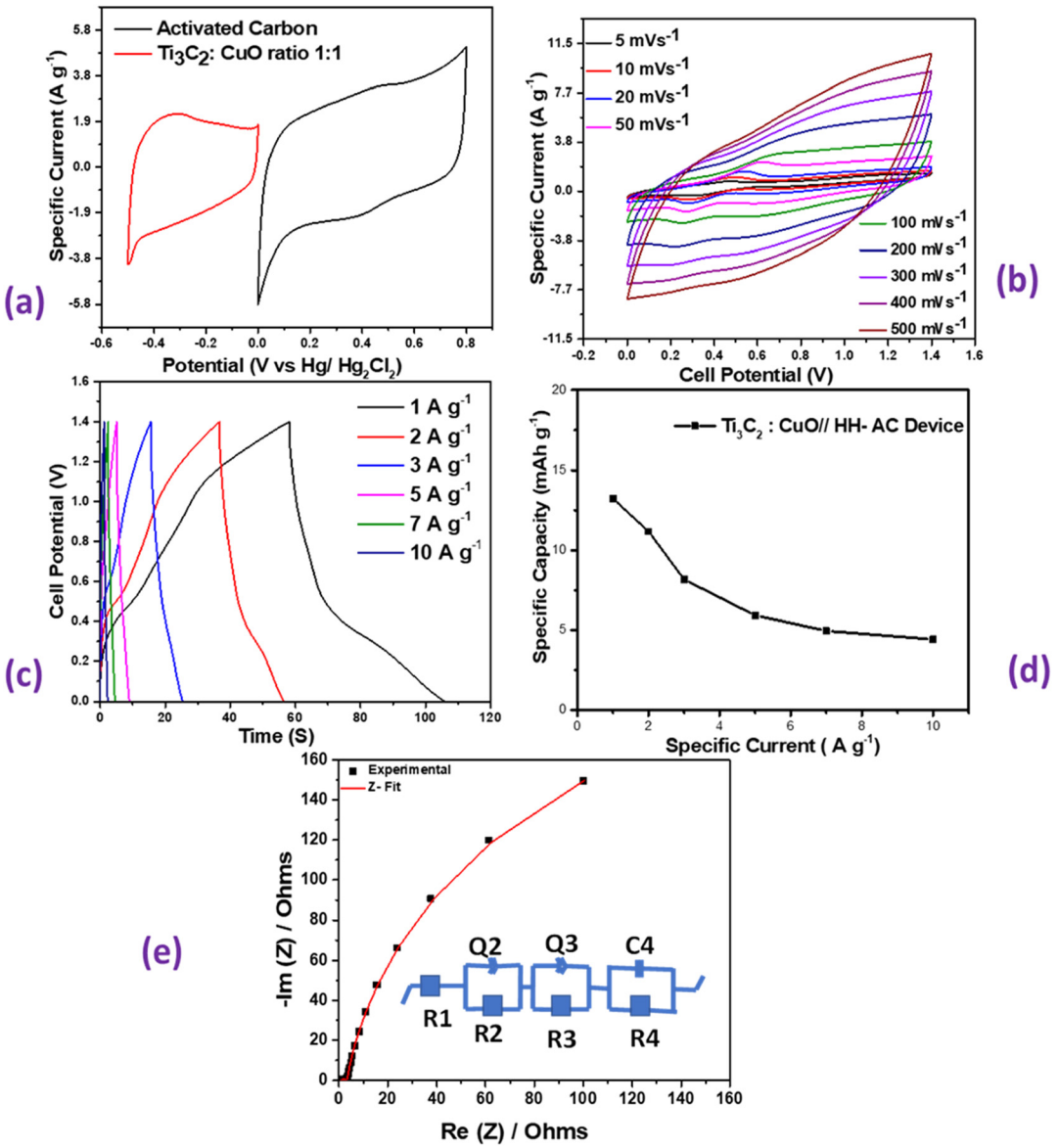

Fig. 10 (a) CV curves of the Ti_3C_2 : CuO QDs (1 : 1) composite and human hair-derived activated carbon recorded at 20 mV s^{-1}, (b) CV curves of Ti_3C_2 : CuO QDs//human hair-derived activated carbon at distinct scan rates of the asymmetric device, (c) GCD profiles of Ti_3C_2 : CuO QDs//HH-AC at various specific currents of the asymmetric device, (d) specific capacity *vs.* specific current of the asymmetric device, (e) the fitted EIS Nyquist plot for the Ti_3C_2 : CuO QDs//HH-AC asymmetric device with an equivalent circuit of the fitted Nyquist plot of the Ti_3C_2 : CuO QDs//HH-AC asymmetric device shown as an inset.

approximately 0.8 Ω. This low R_s value indicates minimal internal resistance and efficient transport within the device. The semicircle in the high-frequency region was relatively small, indicating an efficient charge transfer resistance (R_{ct}) of 2.1 Ω. The equivalent circuit fitting (inset of Fig. 10(e)) used to fit the EIS data comprises resistive elements (R_s = $R1$ and R_{ct} = $R3$), constant phase elements (CPEs) $Q2$ and $Q3$, and an additional interfacial resistive element ($R2$), which accounts for electrode porosity and interfacial inhomogeneity. The good agreement between the fitted (R_s = 0.95 Ω, R_{ct} = 2.35 Ω) and experimental (R_s = 0.8, R_{ct} = 2.1 Ω) data validates this model. Specifically, the presence of multiple constant phase elements reflects non-ideal capacitive behavior caused by surface roughness, distributed pore sizes, and interfacial heterogeneity.[51] $C4$ and $R4$ are defined as diffusion capacitance and resistance, respectively.[51,52]

Fig. 11(a) displays the continuous charge–discharge cycling performance of Ti_3C_2 : CuO QDs//HH-AC over 10 000 cycles at 10 A g^{-1}; the device maintains 82.6% capacitance retention with a nearly constant coulombic efficiency (CE) of 94.8%. The stable CE throughout the test indicates highly reversible charge storage reactions and minimal parasitic reactions.[53] The gradual – rather than abrupt – capacity fade suggests slow morphological relaxation rather than structural failure.[54,55] Fig. 11(b) shows cyclic voltammograms recorded at 20 mV s^{-1} before and after the 10 000-cycle test, which largely overlap in

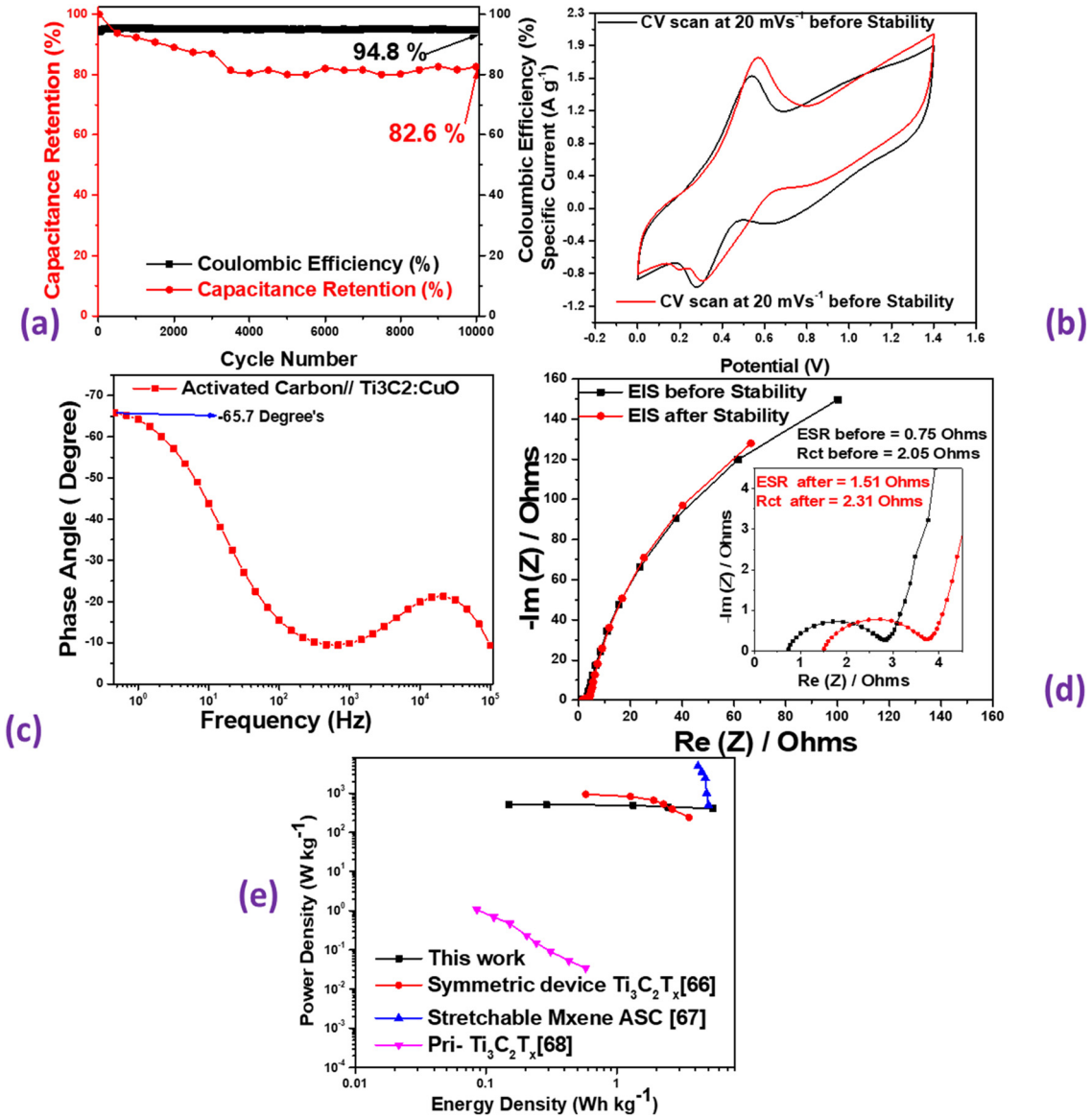

Fig. 11 (a) Cycling performance of Ti_3C_2 : CuO QDs//HH-AC over 10 000 cycles at 10 A g^{-1}, (b) CV scan of Ti_3C_2 : CuO QDs//HH-AC at 20 mV s^{-1}, (c) the Bode plot of Ti_3C_2 : CuO QDs//HH-AC, (d) EIS Nyquist plot of Ti_3C_2 : CuO QDs//HH-AC before and after 10 000 cycles at 5 A g^{-1} with the enlarged high-frequency region shown as an inset and (e) the power density *vs.* energy density plot comparing the performance of the device with other devices.

shape and area, retaining the quasi-rectangular profile with shallow redox humps. This persistence confirms that (i) the HH-AC electrode continues to provide robust double-layer storage across the full voltage window and (ii) the Ti_3C_2 : CuO negative electrode preserves fast, reversible faradaic contributions.[56,57] The absence of severe distortion or peak migration after cycling indicates minimal loss of accessible surface and stable interfacial chemistry.[58]

In Fig. 11(c), the device shows a maximum phase angle of 65.7° at low frequency, reflecting predominantly capacitive behavior with a modest resistive component, which is expected for an asymmetric configuration. The progressive decrease of phase angle with frequency indicates the transition from ideal capacitive storage (ion diffusion governed) to resistive/kinetic limitations at higher frequencies.[59] The smooth dispersion without sharp resonances implies a broad distribution of relaxation times associated with hierarchical porosity.[60] The Nyquist plots in Fig. 11(d) display a small high-frequency intercept and a modest semicircle followed by a steep low-frequency line, consistent with the equivalent circuit behavior typical of hybrid supercapacitors.[61,62] Quantitatively (inset), the equivalent series resistance increases from ~0.8 Ω (before the long cycling test) to ~1.5 Ω (after the long cycling test), attributable to minor increases in contact/electrolyte resistance during long cycling (*e.g.*, interfacial compaction or slight electrolyte depletion).[63]

The charge-transfer resistance (R_{ct}), obtained from the Nyquist plot in Fig. 11(d), changes only slightly from approximately 2.05 Ω

Table 1 Comparison of MXene-based CuO and other hybrid materials reported in the literature

Material	Synthesis/method	Electrochemical performance	Key advantages	Ref.
Copper cobalt-based ternary phosphide (CCP)	Gas–solid thermal route	Capacity retention of 94.4% over 5000 cycles High energy and power density values of 129.15 W h kg^{-1} and 66.4 kW kg^{-1}	3D spatial morphology with a hierarchical architecture and porosity	69
Vanadium nitride thin film-coated graphite	Reactive direct current (DC) magnetron sputtering method	Capacitance of 91 mF cm^{-2} Cycling stability with >64% capacitance retention after 2000 cycles	Flexible, thin, light-weight, electrically conductive, cost-effective, and easy to fabricate	70
CuCo-carbonate double hydroxide	Modified anion exchange process	5000 cycles with 94.2% capacitance retention Device with a high specific capacity of 287.35 C g^{-1} at 7 A g^{-1}	Highly porous nature in nanospikes of 3D urchin CCO structures	71
Copper cobalt-based sulfide ($CuCo_2S_4$)	Hydrothermal anion-exchange process	$CuCo_2S_4$ capacitance of 966–676.8 C g^{-1} and 70.15% retention CuS/CoS delivered 455.3–278.8 C g^{-1} and 61.23% retention	Spinel crystalline structure with unique dendrite morphology	72
Ti_3C_2/CuO QDs (this work)	Hybridization strategy	108.1 F g^{-1} capacitance And a device with a high coulombic efficiency of 94.8%, excellent cycling stability with 82.6% capacitance retention after 10 000 cycles	Synergistic electron transport + nanoscale active sites Layer intercalation	This work

to 2.31 Ω after cycling, indicating that the electrode maintains efficient interfacial charge transfer. This minimal increase in R_{ct} can be attributed to the stable redox activity of CuO and the conductivity of the Ti_3C_2 framework, which together preserve the integrity of the electrode–electrolyte interface. The nearly vertical low-frequency tail further confirms that ion diffusion through the Ti_3C_2 : CuO structure and within the HH-AC macro/mesoporous network remains efficient after prolonged cycling. These characteristics collectively explain the high coulombic efficiency and moderate capacitance decay observed.[64,65] Fig. 11(e) displays the Ragone plot, which was calculated using eqn (5) and (6) to demonstrate the specific energy and specific power of the device incorporating Ti_3C_2 : CuO. At a specific current of 1 A g^{-1}, the device delivers a specific energy of 5.4 W h kg^{-1} and a corresponding specific power of 410 W kg^{-1}. These values are slightly higher than those previously reported for symmetric $Ti_3C_2T_x$ supercapacitors,[66] stretchable MXene-based ASCs,[67] and pristine $Ti_3C_2T_x$ devices,[68] as shown in the Ragone plot. The present device demonstrates superior performance by achieving both high specific energy and power, placing it among the top-performing systems within the Ragone plot comparison space. This improvement arises from the synergistic pairing of the conductive Ti_3C_2 : CuO negative electrode with the high-surface-area HH-AC positive electrode, which collectively enables efficient charge transfer and a wider operating voltage window. Table S1 tabulates the experimental values obtained in this work. Furthermore, a comparison of the material reported in this work with different materials used for energy storage is shown in Table 1 as an inspiration to further modify its morphological structure, which plays a key role in electrochemical energy storage.

Table 1 presents a comparative overview of MXene–CuO and related hybrid materials, highlighting key structural features and electrochemical performance. The results indicate that integrating CuO quantum dots with conductive MXene frameworks enhances charge transport and increases electrochemically active sites, thereby improving energy storage performance. MXene's structural versatility also supports applications beyond energy storage, such as photocatalytic removal of water-borne contaminants.[73] Related studies on self-powered water splitting[74] and high-areal-capacity lithium-ion electrodes,[75] although not MXene-based, provide complementary design insights into interface engineering and electrode architecture. These findings guide the rational design of next-generation MXene-based composites with improved electrochemical efficiency and stability.

4. Conclusion

In this work, a Ti_3C_2 : CuO QDs composite was successfully synthesized, investigated, and integrated with a hierarchically porous activated carbon (HH-AC) to construct an asymmetric supercapacitor device. The combination of conductive MXene nanosheets and redox-active CuO provided abundant electroactive sites and efficient charge transport when tested in three-electrode systems. The capacitance of MXene improved by 46% from 74.2 to 108.1 F g^{-1}. From characterization results, it was observed that the quantum dots modified the surface of MXene layers, intercalation also took place, and the conduction of the material improved. The assembled asymmetric supercapacitor device was very stable, with HH-AC offering fast ion-buffering and double-layer storage. As a result, the device delivered outstanding cycling durability (82.6% capacitance retention after 10 000 cycles at 5 A g^{-1}) and near-ideal coulombic efficiency (~95%). Electrochemical impedance analysis further confirmed the minimal growth of charge-transfer resistance and stable ion diffusion within the porous framework, underpinning the long-term reliability of the system. These findings demonstrate that coupling MXene-based pseudocapacitive electrodes with engineered carbon counterparts is a potentially effective strategy to overcome the energy–power limitations of conventional supercapacitors. Beyond validating Ti_3C_2 : CuO as a robust negative electrode, this study provides a platform for the rational design of next-generation asymmetric supercapacitors with higher energy density, power density, and cycling stability, suitable for practical energy storage applications.

Conflicts of interest

There are no conflicts to declare.

Data availability

Data will be available from the authors upon request.

Supplementary information (SI) is available. See DOI: https://doi.org/10.1039/d6nj00232c

Acknowledgements

This study was supported by the South African Research Chairs Initiative of the Department of Science and Technology, South Africa, and the National Research Foundation of South Africa (Grant No. RNESW240307208354). All observations and results presented in this work are those of the authors, and the NRF does not accept any liability in this regard. Mpho Rantsotlhe acknowledges financial support from the NRF through the SARChI chair in Nanomaterials for Energy storage and Water purification.

References

1 F. Perera and K. Nadoeau, *N. Engl. J. Med.*, 2022, **386**, 2303–2314.
2 F. Perera, *Int. J. Environ. Res. Public Health*, 2018, **15**, 16.
3 U.S. Energy Information Administration, *Short-Term Energy Outlook*, U.S. Department of Energy, 2023.
4 A. Dutta, S. Mitra, M. Basak and T. Banerjee, *Energy Storage*, 2023, **5**, e339.
5 J. Mitali, S. Dhinakaran and A. A. Mohamad, *Energy Storage Sav.*, 2022, **1**, 166–216.
6 T. H. Murray, *Science*, 2014, **343**, 1208–1210.
7 D. J. Tarimo, *et al.*, *J. Energy Storage*, 2022, **51**, 104378.
8 J. Libich, *et al.*, *J. Energy Storage*, 2018, **17**, 224–227.
9 T. M. Masikhwa, *et al.*, *J. Colloid Interface Sci.*, 2017, **488**, 155–165.
10 B. Pal, *et al.*, *Nanoscale Adv.*, 2019, **1**, 3807–3835.
11 W. Wei, *et al.*, *J. Energy Chem.*, 2020, **48**, 277–284.
12 K. O. Oyedotun, *et al.*, *J. Energy Storage*, 2021, **36**, 102419.
13 Y. Homayouni, J. R. Trump, C. J. Grier, J. Peng, J. J. Giner Sanz and L. Giordano, *J. Phys. Energy*, 2021, **3**, 042006.
14 Z. S. Iro, C. Subramani and S. S. Dash, *Int. J. Electrochem. Sci.*, 2016, **11**, 10628–10643.
15 S. Karthikeyan, *et al.*, *Mater. Today Proc.*, 2020, 3984–3988.
16 A. V. Mohammadi, J. Rosen and Y. Gogotsi, *Science*, 2021, **372**, eabf1581.
17 M. Naguib, M. W. Barsoum and Y. Gogotsi, *Adv. Mater.*, 2021, **33**, 2103393.
18 Y. Gogotsi, *Chem. Mater.*, 2023, **35**, 8767–8770.
19 S. Biswas and P. S. Alegaonkar, *Surfaces*, 2022, **5**, 1–34.
20 Z. Bao, *et al.*, *Chin. Chem. Lett.*, 2021, **32**, 2648–2658.
21 R. Azadvari, *et al.*, *J. Phys. D: Appl. Phys.*, 2024, **57**, ad056c.
22 M. Naguib, *et al.*, *ACS Nano*, 2012, **6**, 1322–1331.
23 D. Momodu, *et al.*, *Electrochim. Acta*, 2021, **388**, 138664.
24 K. O. Oyedotun, *et al.*, *Electrochim. Acta*, 2019, **301**, 487–499.
25 S. Wang, *et al.*, *Chem. Eng. J.*, 2023, **452**, 139512.
26 T. Jiang, Y. Wang and G. Z. Chen, *Small Methods*, 2023, **7**, 2201724.
27 R. A. M. Adam, *et al.*, *Mater. Renewable Sustainable Energy*, 2025, **14**, 294.
28 F. Piri, M. Shafiee Afarani and A. M. Arabi, *Mater. Res. Express*, 2019, **6**, 0650xx.
29 U. Falak, *et al.*, *Ceram. Int.*, 2023, **49**, 21026–21035.
30 F. Liu, *et al.*, *Adsorption*, 2016, **22**, 915–922.
31 V. Presser, *et al.*, *J. Raman Spectrosc.*, 2012, **43**, 168–172.
32 M. Rashad, *et al.*, *J. Nanomater.*, 2013, **2013**, 714853.
33 A. S. Zoolfakar, *et al.*, *J. Mater. Chem. C*, 2014, **2**, 5247–5270.
34 X. Liu, L. Wang, Y. Zhao and H. Wang, *ACS Appl. Mater. Interfaces*, 2016, **8**, 12345–12352..
35 B. Anasori, M. R. Lukatskaya and Y. Gogotsi, *Nat. Rev. Mater.*, 2017, **2**, 16098.
36 M. Naguib, *et al.*, *ACS Nano*, 2012, **6**, 1322–1331.
37 K. Krishnamoorthy, *et al.*, *J. Mater. Chem. A*, 2017, **5**, 5726–5736.
38 A. M. Navarro-Suárez, *et al.*, *Batter. Supercaps*, 2018, **1**, 33–38.
39 R. L. Fomekong, *et al.*, *J. Mater. Chem. C*, 2023, **11**, 6034–6045.
40 H. Siddiqui, *et al.*, *J. Mater. Sci.*, 2018, **53**, 8826–8843.
41 K. N. Rathod, *et al.*, *Int. J. Nanosci.*, 2017, **16**, 1750019.
42 H. P. Klug and L. E. Alexander, *X-ray Diffraction Procedures*, Wiley, 1974.
43 J. Liew, *et al.*, *Mater. Sci. Eng., B*, 2025, **314**, 118076.
44 X. Li, *et al.*, *Mater. Chem. Phys.*, 2021, **268**, 124748.
45 W. Ma, *et al.*, *RSC Adv.*, 2022, **12**, 3554–3560.
46 M. I. H. Protyai and A. Bin Rashid, *Heliyon*, 2024, **10**, e37030.
47 M. P. Geetha, *et al.*, *Cogent Eng.*, 2020, **7**, 1783102.
48 G. R. Berdiyorov, *EPL*, 2015, **111**, 67002.
49 V. Senthilkumar, *et al.*, *RSC Adv.*, 2015, **5**, 20545–20553.
50 S. Trasatti and O. A. Petrii, *J. Electroanal. Chem.*, 1992, **327**, 353–376.
51 B. Csomós and D. Fodor, *Hung. J. Ind. Chem.*, 2020, **48**, 33–41.
52 R. N. Vyas and B. Wang, *Int. J. Mol. Sci.*, 2010, **11**, 1956–1972.
53 B. E. Conway, *Electrochemical Supercapacitors*, Springer, 1999.
54 P. Simon and Y. Gogotsi, *Nat. Mater.*, 2008, **7**, 845–854.
55 Y. Pan, K. Xu and C. Wu, *Nanotechnol. Rev.*, 2019, **8**, 299–314.
56 M. R. Lukatskaya, *et al.*, *Science*, 2013, **341**, 1502–1505.
57 M. Q. Zhao, *et al.*, *Adv. Mater.*, 2015, **27**, 339–345.
58 G. R. Ravi, *et al.*, *Energy Storage Devices*, IntechOpen, 2024.
59 J. R. Miller and P. Simon, *Science*, 2008, **321**, 651–652.
60 J. Chmiola, *et al.*, *Science*, 2006, **313**, 1760–1763.
61 J. Bisquert, *J. Phys. Chem. B*, 2002, **106**, 325–333.
62 A. Lasia, *Electrochemical Impedance Spectroscopy*, Springer, 2014.
63 B. W. Pratama, *et al.*, *J. Multidiscip. Appl. Nat. Sci.*, 2025, **5**, 408–418.
64 C. Ferrara, *et al.*, *Curr. Opin. Electrochem.*, 2021, **29**, 100764.

65 M. Boota, *et al.*, *Adv. Mater.*, 2016, **28**, 1517–1522.
66 A. M. Navarro-Suárez, *et al.*, *Electrochim. Acta*, 2018, **259**, 752–761.
67 J. Tang, *et al.*, *Energy Storage Mater.*, 2020, **32**, 418–424.
68 T. H. Chang, T. Zhang, H. Yang, K. Li, Y. Tian, J. Y. Lee and P. Y. Chen, *ACS Nano*, 2018, **12**, 8048–8059, DOI: 10.1021/acsnano.8b02908.
69 R. Arulraj, A. George and M. Kundu, *ACS Appl. Nano Mater.*, 2024, **7**, 14297, DOI: 10.1021/acsanm.4c01807.
70 A. Ramadoss, A. Mohanty, K. G. Saravanan, M. Kundu, S. Z. Noby, K. Kirubavathi, K. Selvaraju and L. S. Mende, *Ionics*, 2022, **28**, 2513–2524, DOI: 10.1007/s11581-022-04529-z.
71 A. George and M. Kundu, *ACS Omega*, 2023, **8**, 17028–17042, DOI: 10.1021/acsomega.3c01211.
72 A. George and M. Kundu, *Energy Fuels*, 2022, **36**, 12327–12340, DOI: 10.1021/acs.energyfuels.2c02438.
73 K. Li, X. Lu, Y. Zhang, K. Liu, Y. Huang and H. Liu, *Environ. Res.*, 2020, **185**, 109409, DOI: 10.1016/j.envres.2020.109409.
74 M. Mushtaq, Z. Zhu, H. Yang, Z. Khanam, Y. W. Hu, S. Mathi, Z. Wang, M. S. Balogun and Y. Huang, *Small*, 2025, **21**, e2409418, DOI: 10.1002/smll.202409418.
75 G. Li, T. Ouyang, T. Xiong, Z. Jiang, D. Adekoya, Y. Wu, Y. Huang and M.-S. Balogun, *Carbon*, 2021, **174**, 515–525, DOI: 10.1016/j.carbon.2020.12.027.

